Proceedings of the Thirty-sixth (2026) International Ocean and Polar Engineering Conference
Orlando, Florida, USA, May 31-June 5, 2026

ISBN 978-1-880653-72-2; ISSN 1098-6189
www.isope.org

Analysis of the Integrated Coupled Response of a 15-MW Floating Wind Turbine Subjected to Focused Wave Actions

*Min Li, Weiwen Zhao, Decheng Wan**

Computational Marine Hydrodynamics Lab (CMHL), School of Ocean and Civil Engineering,
Shanghai Jiao Tong University, Shanghai, China
*Corresponding Author

ABSTRACT

This study analyzes the air-gap response of a floating wind turbine platform under extreme focused waves. Numerical simulations show that the air gap systematically decreases with increasing wave height. The global minimum consistently occurs in front of the lower right column, forming a high-risk zone for slamming. This phenomenon is attributed to the coupling between platform heave and pitch-roll motions. The research reveals the evolution mechanism of the air gap under coupled dynamic effects. It provides a basis for the freeboard design and local reinforcement of floating wind turbines.

KEY WORDS: Floating wind turbine; focused wave actions; 15MW; FEWT-SJTU; motion response.

INTRODUCTION

Floating offshore structures, especially floating offshore wind turbine (FOWT) platforms of 15MW and above, are key equipment for harnessing deep-sea wind energy resources. A core parameter for their structural safety is the "air gap", defined as the minimum vertical distance between the underside of the platform and the wave surface. This parameter is critical for assessing a platform's ability to withstand extreme sea states. A negative air gap directly leads to deck slamming, which can cause local damage and even platform instability. (Kaiser et al., 2009; Zhang et al., 2024) Among various extreme sea conditions, freak waves are a primary factor inducing the most hazardous air gap conditions and the largest wave impact loads. This is due to their characteristics of sudden occurrence, enormous wave amplitude, and highly concentrated energy. Unlike regular waves, freak waves can form an exceptionally large crest within a short time, exerting a powerful transient impact on the structure. More importantly, for large FOWT platforms, the occurrence of the most critical air gap is not caused directly by a single wave crest alone. Instead, it results from the nonlinear superposition and dynamic coupling of three factors: the large amplitude of the freak wave, the platform's own complex multi-degree-of-freedom coupled motions, and the instantaneous wave surface profile. Therefore, systematically investigating the mechanism of how freak wave amplitude variations influence the spatiotemporal distribution of the air gap response around the platform is of significant importance. This research is crucial for ensuring the safe operation of large floating wind turbines under extreme sea conditions.

Numerous scholars have conducted research on the dynamic response of floating wind turbine platforms under extreme wave actions. Early studies primarily focused on the distribution characteristics of the air gap under regular waves. For instance, Zhu et al. (2022) experimentally investigated the slamming characteristics of breaking regular and irregular waves on a monopile offshore wind turbine. Zhang et al. (2017) performed a global hydrodynamic analysis of a semi-submersible floating production unit. Their work revealed that wave directionality significantly affects the air gap, with short-crested waves leading to a more uniform air gap distribution. However, this study did not address the extreme nonlinear effects of freak waves. Liu et al. (2022) further utilized an OpenFOAM-based numerical wave tank. They demonstrated that wave reflection and energy locking between columns cause an uneven distribution of wave run-up height. This effect can be amplified in focused wave scenarios, increasing the slamming pressure to 46.59 MPa. This highlights the structural risk associated with an insufficient air gap. Freak waves, characterized by a sudden increase in wave height and concentrated energy, have a more pronounced transient compression effect on the air gap. Huo et al. (2021) conducted a combined CFD and experimental study. They found that freak waves significantly amplify the slamming pressure on a semi-submersible platform. The maximum pressure near the base of the column reached 137.2 kPa, which is 287.68% of the value under normal conditions. Furthermore, the slamming pressure on the rear columns was 192% to 220% higher than on the front columns. This was accompanied by negative air gaps and significant wave run-up, highlighting strong nonlinear interactions. Further research by Huo et al. (2023) indicated that the slamming pressure under freak waves exhibits a double-peak characteristic and decreases along the structural height. The secondary impact pressure reached 88.6 kPa, doubling the risk of deck impact when the air gap is insufficient. Numerical simulations by Xu et al. (2024) showed that freak waves can amplify the surge, heave, and pitch motions by 191.22%, 116.86%, and 106.14%, respectively, compared to random waves. The motion energy is concentrated at the wave focusing moment. This change in platform attitude indirectly compresses the air gap. Similarly, Meng et al. (2025) studied a 15MW semi-submersible floating wind turbine. Their research confirmed that freak waves increase the pitch response by 94%. Wavelet energy was concentrated at the wave frequency and the structure's natural frequency, lasting for about 20 wave periods. This exacerbates the dynamic fluctuation of the air gap. Zeng et al. (2023) discovered that freak waves amplify motion amplitudes (surge +44%, pitch +94%). This leads to a 41% increase in nacelle acceleration peak, affecting power generation stability. This indirectly reflects how sudden air gap changes affect the superstructure. Liu and Yu (2024) focused on the coupled scenario of freak waves and mooring line failure. They pointed out that the peak surge response increases by 191%, and mooring tension rises by 220%. Such large-amplitude motions may further deteriorate air gap conditions through platform drift.

Currently, numerous studies have analyzed wave loads or platform motion responses through numerical simulations or model tests. However, research on floating platforms suitable for 15-MW-class large-scale wind turbines still has limitations. Specifically, how the variation in amplitude of focused waves, which can accurately simulate extreme wave events, systematically affects the spatial distribution pattern and evolution process of the air gap for such large platforms has not been thoroughly investigated. This study aims to systematically explore how changes in the coupled dynamic response of the platform and the surrounding transient flow field determine the degradation pattern of the minimum air gap, its spatial distribution characteristics, and the formation mechanism of local high-risk zones.

This study takes a typical semi-submersible floating offshore wind turbine platform as the object. A pure wind condition and a series of focused wave conditions with different amplitudes are set. The structure of this paper is as follows: Section 2 details the numerical calculation model and the air gap calculation method. Section 3 introduces the main parameters of the platform and the condition settings. Section 4 presents and analyzes the results of air gap response, platform motion response, and flow field details under different conditions. A comprehensive discussion is provided, explaining the potential hazardous areas and their causes.

METHODOLOGY

This study is based on the open-source software OpenFOAM, and the CFD numerical simulations are performed using the self-developed aero-hydro-mooring coupled solver FEWT-SJTU. The aerodynamic module employs an unsteady actuator line model, the hydrodynamic module is derived from the in-house solver naoe-FOAM-SJTU for solving the six-degree-of-freedom motion of the platform, and the mooring module is based on the piecewise extrapolation method for the analysis of mooring chains. The self-developed solver used for motion response calculations has been validated in prior studies (Cheng et al., 2019). Therefore, a separate validation is not presented here, allowing the focus to remain on the new application and results.

Governing Equation

To solve for unsteady incompressible viscous flow, the governing equations employed are the incompressible two-phase Navier–Stokes equations:

$$\nabla \cdot \boldsymbol{U} = 0 \tag{1}$$

$$\frac{\partial \rho \boldsymbol{U}}{\partial t} \nabla \cdot (\rho \boldsymbol{U}\boldsymbol{U}) = -\nabla p_{\mathrm{d}} - \boldsymbol{g} \cdot \boldsymbol{x} \nabla \rho + \nabla(\mu_{\mathrm{eff}} \nabla \boldsymbol{U}) + \boldsymbol{f}_{\sigma} + \boldsymbol{f}_{\mathrm{s}} + \boldsymbol{f}_{\varepsilon} \tag{2}$$

where $\boldsymbol{U}$ is the velocity field; ρ is the density of the liquid or gas; t is time; p_d is the dynamic pressure, defined as the total pressure minus the hydrostatic pressure; $\boldsymbol{g}$ is the gravitational acceleration vector; $\boldsymbol{x}$ is the position vector; μ_{eff} is the effective dynamic viscosity, expressed as $\mu_{eff} = \rho(\nu + \nu_t)$, in which ν and ν_t are the kinematic viscosity and turbulent eddy viscosity, respectively, with ν_t obtained from a turbulence model; $\boldsymbol{f}_\sigma$ is the surface tension source term, which acts only at the gas–liquid interface; $\boldsymbol{f}_s$ is the wave damping source term, active only within the wave damping zone; and $\boldsymbol{f}_\varepsilon$ is the wind-turbine body force source term, resulting from the projection of aerodynamic forces from the turbine blades onto the flow field. In the full-scale simulations considered here, the effect of surface tension is secondary; it is retained primarily for the physical completeness of the model and the numerical stability of the interface capture. The turbulence closure is provided by the SST k–ω model.

Coupled strategy

The coupling among the wind turbine, floating platform, and mooring system is achieved through the transfer of forces, displacements, and velocities. The aerodynamic loads are calculated based on the unsteady actuator line model, which accounts for variations in blade position and incoming wind speed caused by platform motion. The six-degree-of-freedom motion equations of the floating platform are solved with consideration of the impact from the aerodynamic loads of the wind turbine. Simultaneously, the platform motion response provides positional input for the mooring attachments in the mooring system solution, and the resulting mooring tensions are also fed back into the platform motion equations. Fig. 1 outlines the coupled computational approach integrating the hydrodynamic performance of the floating platform and mooring system with the aerodynamic performance of the wind turbine.

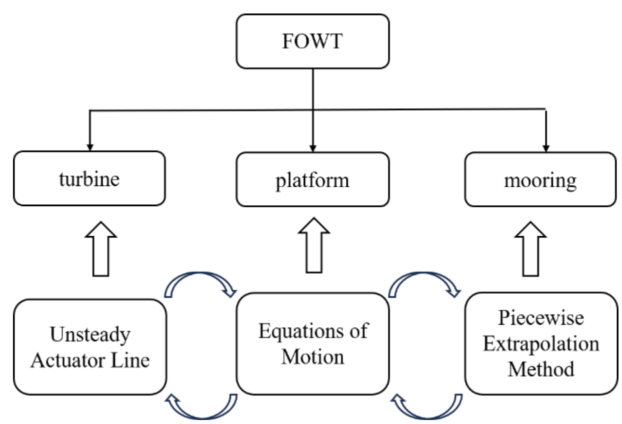

Fig. 1 Fluid-structure coupling calculation of wind turbine blades

Methodology for Airgap Calculation

The instantaneous position of point A is updated in real time based on the initial center of gravity G of the entire floating wind turbine structure, the initial position C of the rotor disc plane, and the initial position A of the highest point on the floating structure column. According to the six-degree-of-freedom rigid-body motion theory, the updating formula for the coordinates of point A is obtained as:

$$\begin{pmatrix} Ax \\ Ay \\ Az \end{pmatrix} = R \begin{pmatrix} Cx - Gx - r\sin\phi \\ Cy - Gy \\ Cz - Gz - r\cos\phi \end{pmatrix} + \begin{pmatrix} d_x \\ d_y \\ d_z \end{pmatrix} \tag{3}$$

$$R = \begin{bmatrix} \cos\theta_y + \cos\theta_z & -\sin\theta_z & \sin\theta_y \\ \sin\theta_z & \cos\theta_x + \cos\theta_z & -\sin\theta_x \\ -\sin\theta_y & \sin\theta_x & \cos\theta_x + \cos\theta_y \end{bmatrix} \tag{4}$$

where d and θ denote the translational and rotational displacements of the floating wind turbine, respectively; φ represents the tilt angle of the rotor disc at the initial time, which accounts for its influence on calculating the position coordinates of point A; and r is the rotor radius. The formula for calculating the air gap is:

$$a(x,y,t) = A(x,y,t) - \eta(x,y,t) \tag{5}$$

where $a(x,y,t)$ denotes the air gap at any spatial point near the wind turbine foundation platform. Based on the time history of the position coordinates of the highest point $A(x,y,t)$ on the floating structure column and the wave surface elevation $\eta(x,y,t)$ at the corresponding location, the time history of the air gap $a(x,y,t)$ at any point near the wind turbine foundation platform can be obtained.

NUMERICAL SETUP

Wind turbine

The wind turbine employed in this study is the IEA 15 MW reference model, which features three blades with a rotor diameter of 240 meters. It operates with a rated wind speed of 10.59 m/s, a hub height of 150 meters, and a rated rotational speed of 7.56 revolutions per minute. Further details and a full set of parameters can be found in Gaertner et al. (2020).

Computational domain and mesh

The computational domain is illustrated in Fig. 2, with dimensions of 1200 meters in length, 702 meters in width, and 590 meters in height. The wind turbine is situated 240 meters downstream from the inlet boundary. The top boundary and the bottom boundary is set as a slip condition, and the left and right sides are defined by symmetry boundary conditions. The incoming wind is introduced by specifying a velocity inlet boundary condition at the domain inlet.

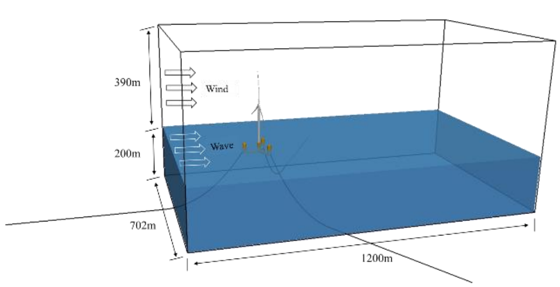

Fig. 2 Computational domain

The computational domain grid is depicted in Fig. 3, with grids uniformly distributed in the x, y, and z directions. To ensure accurate capture of flow field changes near the wind turbine and within the wake region while minimizing computational load, we initially performed grid refinement over a larger area and subsequently conducted further refinement in a finer area. The total number of grids utilized is 3.22 million. The simulation duration is set at 300 seconds, with a time step of 0.01 seconds selected for the calculations.

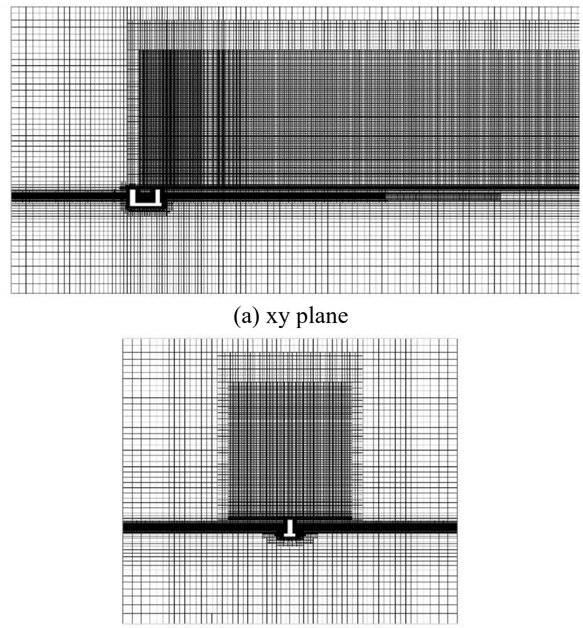

(a) xy plane

(b) yz plane

Fig. 3 Computational meshes

Condition parameter setting

Four operational cases are defined in this study, as shown in Table 1, to investigate the influence of different wave heights on the wind turbine response under identical wind and wave-focusing conditions. The wind speed is kept constant at the rated wind speed of 10.59 m/s in all cases. The wave focal point is set at the coordinate origin (0, 0, 0), which corresponds to the center column of the platform, and the focal time is 150 s. The wave conditions are configured as follows: no waves in Case1, a significant wave height of 3.8 m in Case2, 5.4 m in Case3, and 7.6 m in Case4.

Table 1. Specifications for simulation cases

Margins	wind speed (m/s)	wave height (m)	Focusing location	Focusing time
Case1	10.59	/	/	/
Case2	10.59	3.8	(0, 0, 0)	150s
Case3	10.59	5.4	(0, 0, 0)	150s
Case4	10.59	7.6	(0, 0, 0)	150s

Based on the dimensions of the floating platform, a regular array of measurement points is arranged within a square domain that encloses the main structure of the platform. Centered on the platform, a square region with a side length of 100 meters is defined, which fully covers the platform and its surrounding flow-critical areas. Inside this region, measurement points are uniformly distributed with a spacing of 4 meters in both longitudinal and transverse directions, forming a structured equally spaced grid. In total, 676 measurement points are arranged, enabling a systematic acquisition of the spatial distribution of the air gap around the platform. The layout of the measurement points is illustrated in Fig. 4.

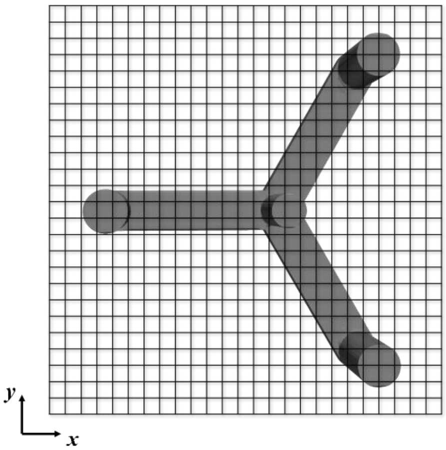

Fig. 4 Layout of measurement points

RESULTS AND DISSCUSSIONS

Airgap response

Fig. 5 presents the distribution of the minimum air gap around the platform under different operating conditions. Overall, the air gap level decreases systematically as wave intensity increases. Under pure wind conditions, the air gap distribution is relatively uniform, ranging from 9.75 m to 19.75 m. The air gap decreases steadily along the incoming flow direction. This is due to the turbine tilting caused by the moment generated between the rotor thrust and the center of gravity. When focused waves are introduced and their amplitude increases, the overall air gap range is significantly compressed. For wave amplitudes of 4 m, 6 m, and 8 m, the lowest air gap occurs near the right-side column of the platform, with minimum values dropping to approximately 8 m, 6.8 m, and 5.2 m, respectively. This indicates that the average distance between the structure and the wave surface is reduced, and the overall probability of wave impact increases.

Secondly, the distribution pattern of the air gap shifts from a uniform gradient to a complex, multi-extremum form. Without waves, the contour lines of the air gap response are sparse and gradual. Under wave action, the spatial distribution of the minimum air gap exhibits steep gradients and multiple local extreme regions. At a wave amplitude of 4 m, isolated low-gap areas have already appeared. As the wave amplitude increases to 6 m and 8 m, the extent of these local low-gap areas expands, the air gap values decrease further, and they coalesce into larger continuous low-gap zones in the figure. Concurrently, the location of the minimum air gap shifts as the wave amplitude changes.

As the wave amplitude increases, the feature that the minimum air gap consistently occurs in the region in front of the lower-right column of the platform becomes more pronounced. This characteristic is primarily induced by wave loads: under pure wind conditions without waves, no distinct localized minimum appears in this area. However, once waves are introduced, as the wave amplitude increases from 4 m to 6 m and 8 m, the air gap at this location decreases progressively to approximately 9.2 m, 8 m, and 6.4 m, respectively. This indicates that the area in front of the lower-right column is the most sensitive region of the structure under wave-induced dynamic response and should be regarded as a critical zone for wave impact risk assessment and structural reinforcement design.

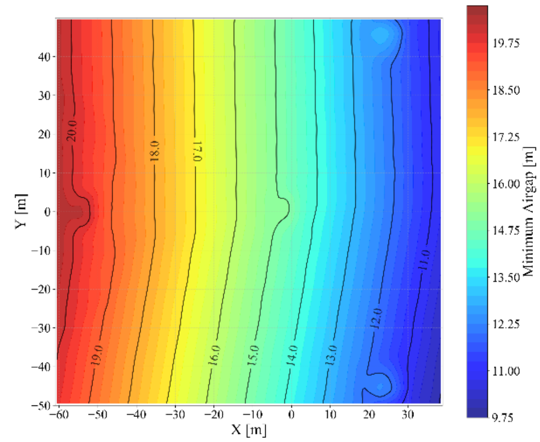

(a) H = 0m

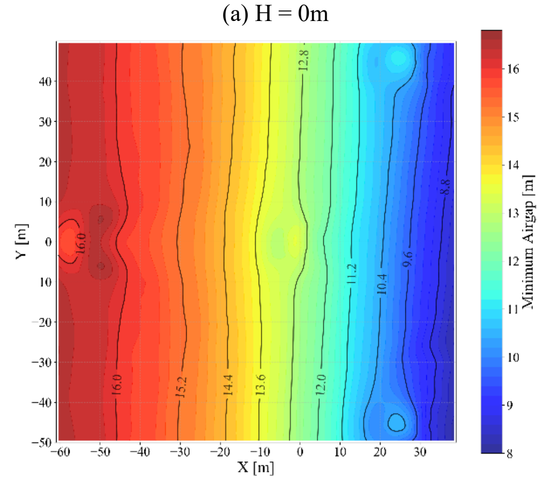

(b) H = 3.8m

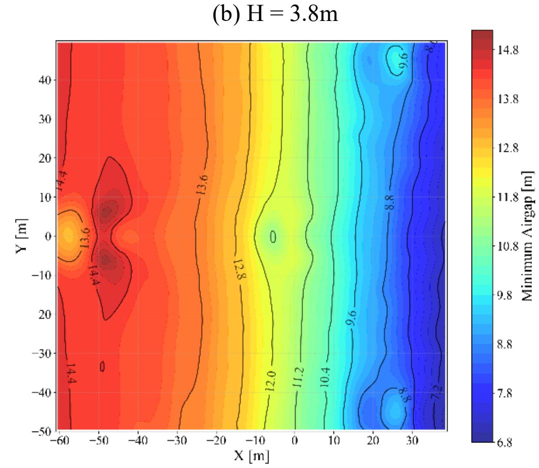

(c) H = 5.4m

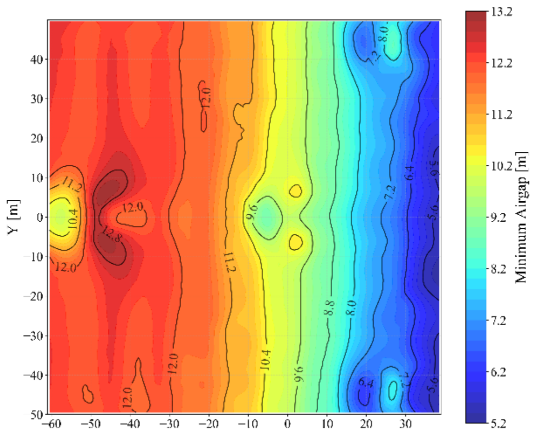

(d) H = 7.6m

Fig. 5 Temporal and spatial distribution of the local attack angle under different amplitudes

Motion response

Fig. 6 presents the time-history comparisons of the platform's heave, pitch, and roll motion responses under four different operational conditions. During the critical period when the focused wave passes the platform (around 150 seconds), the motion patterns can be summarized as follows, which explains the previously observed changes in air gap.

The amplitude of the heave response increases systematically with the wave amplitude. The statistical values of the heave motion response are summarized in Table 2. Its motion amplitude increases significantly from 4.25 m for Case 1 to 8.78 m for Case 4. The increase in heave amplitude directly reduces the clearance between the lower part of the structure and the still water level, which is the primary reason for the overall decrease in the air gap.

The platform maintains a certain pitch angle under all operational conditions, indicating a fixed inclined attitude of approximately 5°–7°. This is caused by the wind thrust moment. When large-amplitude waves pass, distinct periodic fluctuations in the pitch angle occur around 150 seconds. The dynamic pitch motion induced by the waves intensifies this attitude. The statistical values of the pitch motion response are shown in Table 2. The amplitude of the dynamic pitch increases sharply from a negligible 0.07° for Case 1 to 6.73° for Case 4. Furthermore, the motion range is essentially symmetric about zero for Cases 2 to 4, confirming the periodic pitching oscillation induced by the passing waves.

The platform exhibits a small roll angle, with an equilibrium position of approximately 0.5 degrees. This roll angle is primarily induced by asymmetrical loading. The wind load not only generates a pitching moment but, if its point of action has a slight lateral offset relative to the line connecting the platform's center of gravity and center of buoyancy, also produces a steady heeling moment component. When waves pass, the dynamic pitch response superimposes periodic fluctuations on this inclined attitude, causing the column in the lower right area to sink further. This makes the column in the lower right area a combined region of the static lowest point and dynamic sinking. Consequently, the global minimum air gap consistently occurs at this location, and its value decreases significantly as the wave amplitude increases.

Flow Field Details

Fig. 7 presents a comparison of wave surface elevation and morphology near the platform under different operating conditions. Changes in wave surface elevation directly explain the increase in heave motion and the overall reduction in air gap. As wave amplitude increases, the height difference between wave crests and troughs becomes significantly larger, leading to greater heave motion amplitude of the platform. This reduces the vertical distance between the lower surface of the platform and the still water level.

Table 2. Statistical Value of Heave Motion

Margins	Maximum (m)	Minimum (m)	Mean (m)	Amplitude (m)
Case1	23.76	19.51	22.39	4.25
Case2	25.26	20.14	22.52	5.11
Case3	26.58	19.87	22.76	6.71
Case4	28.24	19.46	23.25	8.78

Table 3. Statistical Value of Pitch Motion

Margins	Maximum (m)	Minimum (m)	Mean (m)	Amplitude (m)
Case1	-0.12	-0.19	-0.16	0.07
Case2	1.60	-1.67	-0.06	3.27
Case3	2.49	-2.48	0.00	4.97
Case4	3.38	-3.35	0.07	6.73

Under wave-free conditions, the platform has developed a static pitch inclination due to wind loads. The flow field diagrams show that the wave morphology is visibly asymmetric between the front and rear of the platform. As wave amplitude increases, the difference in water surface height between the front and rear becomes more pronounced. This creates an imbalance in wave forces acting on the front and rear of the platform, which excites dynamic pitch motion. This motion causes the aft of the platform to sink further, resulting in the minimum air gap consistently occurring on that side.

Furthermore, wave-structure interaction complicates the distribution of air gap. In Cases 3 and 4, as waves pass the columns, the water surface morphology becomes highly complex and irregular due to diffraction, reflection, and local run-up, leading to noticeable fluctuations around the columns. Therefore, the instantaneous wave surface under the platform is not planar but exhibits a complex three-dimensional shape. This results in a gradient distribution of air gap and multiple local extreme values in space.

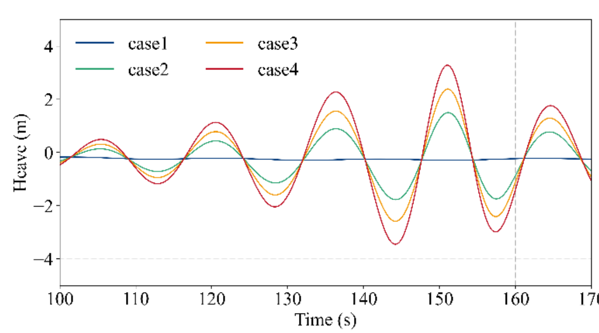

(a) Heave motion

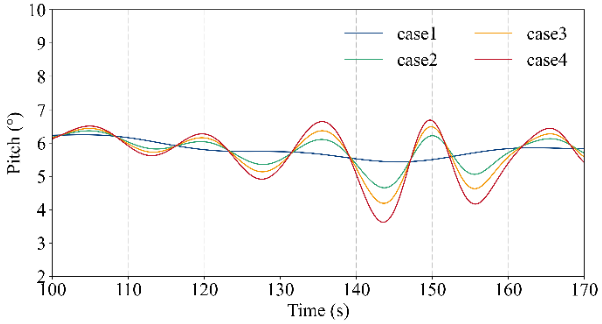

(b) Pitch motion

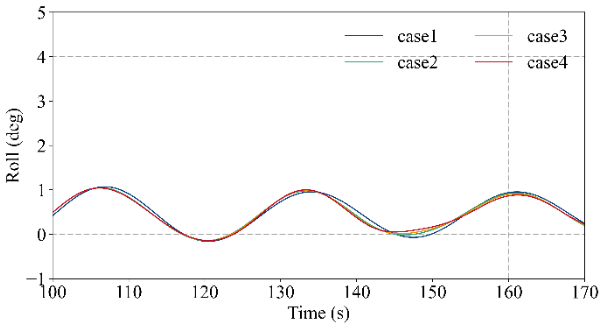

(c) Roll motion

Fig. 6 The heave, pitch, and roll motion responses of the platform.

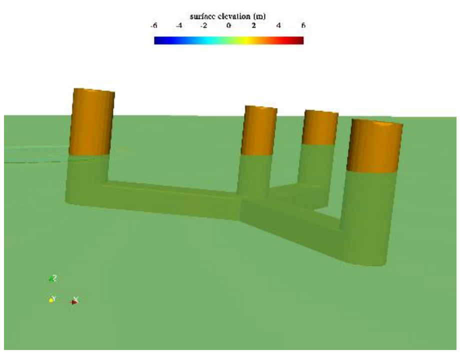

(a) H = 0m

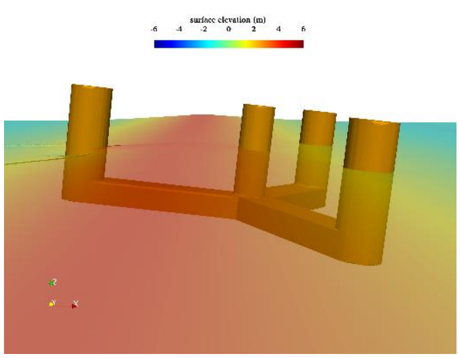

(b) H = 3.8m

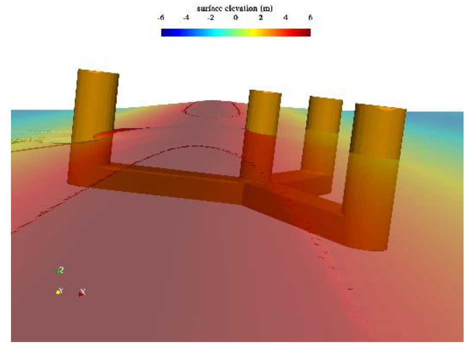

(c) H = 5.4m

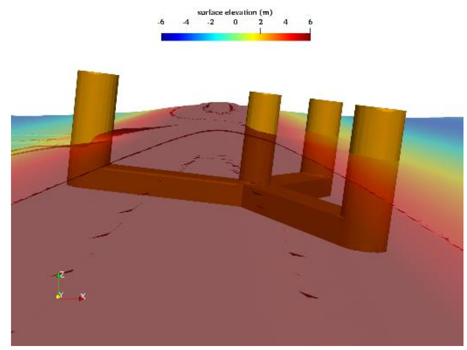

(d) H = 7.6m

Fig. 7 Free-Surface Elevation and Flow Field at the Focusing Instant

CONCLUSIONS

This study analyzes the air-gap response of an offshore structure under focused wave action. By integrating the analysis of air-gap distribution, platform motion, and flow field, three main conclusions are drawn.

First, the air gap decreases systematically with increasing wave amplitude. Its distribution shifts from uniform to a complex pattern featuring gradients and gradually expanding low-air-gap zones. More importantly, the global minimum air gap consistently occurs in front of the lower-right column of the platform. Its value decreases as the wave amplitude increases, dropping to approximately 6.4 m at a wave amplitude of 7.6 m. This indicates that this area is a high-risk zone for wave impact. Second, the reduction in air gap is caused by the coupled effects of platform motion. The increase in wave height leads to a greater heave amplitude, which is the main reason for the overall decrease in air gap. The static inclination of the platform (pitch ~5°–7°, roll ~0.5°) combined with the wave-induced dynamic pitch motion particularly exacerbates the sinking on the right side of the structure. This motion coupling explains why the location of the minimum air gap consistently appears there. Finally, the flow field analysis verifies the above mechanisms. The wave asymmetry in front of and behind the platform creates an unbalanced force couple, exciting the dynamic pitch motion. The complex interaction between the waves and the structure results in a highly irregular instantaneous wave surface. This directly causes the gradients and local extremes in the air-gap distribution.

In summary, the risk of wave impact increases with wave amplitude due to the amplification of platform motion. The area around the lower-right column is the most vulnerable due to the combined static and dynamic tilt. Structural design and assessment must consider such coupled dynamic effects, and local reinforcement should be applied to this critical area. Future work will involve focused wave analysis from other directions, such as beam and oblique seas. Additionally, the effects of air compressibility during wave-impact events will be considered, to more comprehensively evaluate the platform's survivability under multi-directional extreme wave conditions.

ACKNOWLEDGEMENTS

This work was supported by the National Key Research and Development Program of China (2025YFF0519800), to which the authors are most grateful.

REFERENCES

Alkhabbaz, A, Hamza, H, Daabo, AM, Yang, H, Yoon, M, Koprulu, A, and Lee, YH (2024). "The aero-hydrodynamic interference impact on the NREL 5-MW floating wind turbine experiencing surge motion." *Ocean Eng*, 295, 116970.

Cheng, P, Huang, Y, and Wan, D (2019). "A numerical model for fully coupled aero-hydrodynamic analysis of floating offshore wind turbine." *Ocean Eng*, 173, 183-196.

Gaertner, E, Rinker, J, Sethuraman, L, Zahle, F, Anderson, B, Barter, G E, et al (2020). "IEA wind TCP task 37: definition of the IEA 15-megawatt offshore reference wind turbine." National Renewable Energy Lab. (NREL), Golden, CO (United States).

Huo, F, Yang, H, Yao, Z, An, K, and Xu, S (2021). "Study on slamming pressure characteristics of platform under freak wave." *J Mar Sci Eng*, 9(11), 1266.

Huo, F, Zhao, Y, Zhang, J, et al (2023). "Study on wave slamming characteristics of a typical floating wind turbine under freak waves." *Ocean Eng*, 269, 113464.

Huo, F, Zhao, Y, Zhang, J, Zhang, M, and Yuan, Z M (2023). "Study on wave slamming characteristics of a typical floating wind turbine under freak waves." *Ocean Eng*, 269, 113464.

Liu, J, Liu, M, Xiao, L, Wei, H, and Li, X (2023). "Experimental study on the effect of flare barriers on wave run-up and motion response of a semi-submersible platform." *Ocean Eng*,281, 114998.

Liu, B, and Yu, J (2024). "Dynamic Response and Mooring Fracture Performance Analysis of a Semi-Submersible Floating Offshore Wind Turbine under Freak Waves." *J Mar Sci Eng*, 12(8), 1414.

Liu, Y, Xiao, Q, Incecik, A, and Peyrard, C (2019). "Aeroelastic analysis of a floating offshore wind turbine in platform‐induced surge motion using a fully coupled CFD‐MBD method." *Wind Energy*, 22(1), 1-20.

Meng, H, Liu, Y, Tian, D, Long, K, Han, Z, Su, Y, and Sun, K (2025). "Dynamic response of novel floating wind turbine to freak waves during uninterrupted operation." *Renew Energy*, 239, 121984.

Shan, T, Yang, J, Li, X, and Xiao, L (2012). "Review of the research on non-linear wave run-up around columns of deepwater platform." *Ocean Eng*, 30(1), 151-160.

Xu, P, Zhang, Z, Li, S, Song, Q, and Liu, W (2024). "Numerical investigation into the dynamic responses of floating photovoltaic platform and mooring line structures under freak waves." *J Mar Sci Eng*, 12(1), 96.

Zhang, J, Lu, W, Li, X, Guo, X, Tian, X, Yang, J, and Kou, Y (2024). "Assessing air-gap responses of semi-submersible platforms in extreme sea states based on in-situ measurement." *Ocean Eng*, 313, 119378.

Zhang, X, Song, X, Yuan, Z, and You, Y (2017). "Global motion and airgap computations for semi-submersible floating production unit in waves." *Ocean Eng*, 141, 176-204.

Zhu, J, Gao, Y, Wang, L, and Li, W (2022). "Experimental investigation of breaking regular and irregular waves slamming on an offshore monopile wind turbine." *Mar Struct*, 86, 103270.

Zeng, F, Zhang, N, Huang, G, Gu, Q, and He, M (2023). "Dynamic response of floating offshore wind turbines under freak waves with large crest and deep trough." *Energy*, 278, 127679.